Appendix A
Supplementary Materials and Methods

***Dictyostelium* Culture and Microscopy.** *Dictyostelium* cells were grown under axenic conditions in HL5 growth medium in tissue culture plates. We used WT cells (Ax3), myosin II null cells (1) and talin null cells (obtained from M. A. Titus, University of Minnesota, Minneapolis, MN). Aggregation competent cells were prepared by pulsing a 5 x 10^6 cells/ml suspension in Na/K phosphate buffer (9.6 mM KH_2PO_4, 2.4 mM Na_2HPO_4, pH 6.3) with cAMP to a concentration of 30 nM every 6 min for 6 h. Cells were seeded onto the gelatin substrate and allowed to adhere. A drawn glass capillary mounted on a micromanipulator served as the source of chemoattractant (150 μM cAMP in an Eppendorf femtotip, Eppendorf, Germany).

For the image acquisition we used a Nikon TE300 inverted microscope with high numerical aperture lenses and a cooled CCD camera (HQ CoolSnap, Roper Scientific). The microscope was also equipped with a Z-axis drive. A PC running the Metamorph software packet (Molecular Devices, Downington, PA) controlled the entire setup including filter wheels.

Gelatin Gel Fabrication. A 25 mm glass coverslip was mounted to a stainless steel ring using silicon grease (Dow Corning, Midland, Michigan). About 250 μl of a 4% solution of Nabisco Knox gelatin was added and chilled on ice for 1 h. A 1:50 dilution of a 2% carboxylate modified yellow-green latex beads with 0.1 μm diameter (Fluospheres, Molecular Probes, Eugene, Oregon) was added on top of the solidified gelatin for 15 sec. The gels were air dried for 10 min after aspiration of the beads. The gels were melted by briefly placing them on a hot plate and chilled on ice for an additional hour. Before using, they were thoroughly washed with buffer. The resulting gels were between 100 and 200 μm thick in the middle of the dish. The elastic behavior of the gelatin substrate was verified by checking in all cases that the deformation energy in any fixed region of the substrate that is crossed by a cell returns to its baseline after the cell exits the region (see Fig. SI4).

Cell Identification. Cell outlines were determined from differential interference contrast (DIC) images captured using a 40x lens at 2 sec intervals for WT and *talin*$^-$ cells and at 4 sec intervals for *myoII*$^-$ cells. Image processing was performed with MATLAB (Mathworks Inc, Natick, MA). Static imperfections were removed from individual images using the average of the image series. A threshold was applied to the resulting images to extract the most intense features, which were refined using two consecutive image dilations and erosions with structuring elements of increasing size. The sets of connected pixels were detected using BWAERAOPEN and their holes were filled with IMFILL. Finally, the resulting objects were classified using BWLABEL. Figs. SI3*B-D* illustrate these steps. Centroid coordinates (x_c,y_c) and principal axes of each cell were calculated using standard MATLAB functions. Front and back were determined as the two parts in which each cell is divided by its minor axis of inertia, with the front pointing towards the direction of motion. The front can be defined as

$$\xi = [(x - x_c)\cos\alpha + (y - y_c)\sin\alpha][(dx_c / dt)\cos\alpha + (dy_c / dt)\sin\alpha] > 0, \qquad \text{[SI1]}$$

where α is the angle between the x axis and the cell's major axis.

Determination of the Substrate Deformation. We measured the lateral displacements of fluorescent marker particles using an image correlation technique called Particle Image Velocimetry (PIV, (2)). We used the PIV algorithm provided by the software

InsightTM (TSI Incorporated, St Paul, MN) with interrogation windows of 32 x 32 pixels and a 16-pixel overlap, which yields a resolution of 2.75 μm with an average signal-to-noise ratio ~20. In each experimental session, the beads were imaged at the plane where their fluorescence intensity is maximal to minimize systematic errors caused by out-of-focus beads (see Fig. SI5). Fig. SI3*E* shows the fluorescent marker-particles in a region containing a migrating WT cell and Fig. SI3*F* shows the corresponding displacement field. The arrows indicate the absolute value and orientation of the displacements. The magnitude of the displacements is also mapped by the shaded contours and is typically of the order of 0.1 μm.

Calculation of the Traction Forces. We compute the stress field τ applied on the substrate by a cell by solving the elasticity equation of equilibrium for a linear, homogeneous, isotropic, 3D body of finite thickness *h*. Fig. SI3*A* shows a sketch of the problem configuration. The boundary conditions are no slip ($\vec{u} = 0$) at the bottom of the substrate ($z = 0$) and the measured lateral displacements u^0 and v^0 at the average vertical position of the beads, $z = h_0 \leq$ h. We assume periodicity in the horizontal directions. The remaining boundary condition derives from the similar densities of the cells and their surrounding buffer as well as the predominant horizontal orientation of contractile fibers of the cytoskeleton, which suggest that the vertical tensile stresses on the surface of the substrate, $\tau_{zz}(z = h)$, are negligible. We therefore apply the boundary condition $\tau_{zz}(z = h) = 0$.

We solve analytically the elastostatic equation using Fourier series,

$$\bar{\tau}(x,y,z) = \sum_{\alpha=1}^{\infty}\sum_{\beta=1}^{\infty} \hat{\bar{\tau}}_{\alpha\beta}(z) e^{2\pi i\alpha x} e^{2\pi i\beta y} \quad \text{and} \quad \vec{u}(x,y,z) = \sum_{\alpha=1}^{\infty}\sum_{\beta=1}^{\infty} \hat{\vec{u}}_{\alpha\beta}(z) e^{2\pi i\alpha x} e^{2\pi i\beta y}, \qquad \text{[SI2]}$$

where α and β are the *x* and *y* wavenumbers, and $\hat{\bar{\tau}}_{\alpha\beta}(z), \hat{\vec{u}}_{\alpha\beta}(z)$ are the complex Fourier coefficients of $\bar{\tau}$ and $\vec{u}$. The latter are functions of the vertical coordinate and are linearly related to the Fourier coefficients of the horizontal displacements measured at $z = h_0$, $\hat{u}^0_{\alpha\beta}$ and $\hat{v}^0_{\alpha\beta}$. A detailed mathematical derivation of the solution is developed in Appendix B. This solution provides the 3 components of the displacement vector and the 9 components of the stress tensor at all positions inside the three-dimensional domain. We are interested in the tangential stresses at $z = h$, which can be expressed in Fourier space as

$$\begin{pmatrix} \hat{\tau}_{xz}(h) \\ \hat{\tau}_{yz}(h) \end{pmatrix}_{\alpha\beta} = T \begin{pmatrix} \hat{u}^0 \\ \hat{v}^0 \end{pmatrix}_{\alpha\beta}. \qquad \text{[SI3]}$$

The first $N_x \times N_y$ Fourier coefficients of $\vec{u}^0(x,y)$ are computed using a fast Fourier transform (FFT) algorithm after tapering this function with a two-dimensional Hanning window to ensure its periodicity and thus suppress the Gibbs error (3). The tapering window is a square of size (*l*) equal to 6 times the major axis of the cell centered at the centroid of the cell. This is the only information about the geometry of the cell that is required to compute the stresses with our method, which is advantageous because determining the cellular area in contact with the substrate is difficult. When *l* would be larger than the distance from the center of the cell to the boundary of the image, we instead set *l* equal to that distance. The size of the tapering window and the spatial resolution Δ of the displacement field determine $N = l / \Delta$. When *N* was not suitable for the FFT we used the immediate higher number and set the Fourier coefficients to zero for indexes greater than *N*. The tapering also minimizes the disturbances caused by neighboring cells.

The net force $\vec{F}$ exerted on the surface of the substrate is balanced by a force of equal strength and opposite sign applied on its base, given by

$$\vec{F} = \frac{El^2 \hat{\vec{u}}^0{}_{00}}{(1+\sigma)h_0}, \qquad \text{[SI4]}$$

where E is Young's elasticity modulus of the gel and $\hat{\vec{u}}^0{}_{00}$ is the average displacement vector at $z = h_0$. It is useful to decompose this net force into the sum of the pole forces exerted at the front and back halves of the cell, $\vec{F}_f$ and $\vec{F}_b$, where

$$\vec{F}_f = \iint_{\xi>0} \bar{\tau}(x, y, h)dxdy, \qquad \text{[SI5]}$$

and the integral for $\xi < 0$ (see equation SI1) yields $\vec{F}_b$.

The strain work U_s that the cells exert on their substrate is given by

$$U_s = \frac{1}{2}\iiint \bar{\tau} \cdot \bar{\varepsilon} dxdydz = \frac{L_x L_y}{2} \sum_\alpha \sum_\beta \int_0^h \hat{\bar{\tau}}_{\alpha\beta} \cdot \hat{\bar{\varepsilon}}_{\alpha\beta} dz, \qquad \text{[SI6]}$$

where $\bar{\varepsilon}$ is the strain field tensor. The power exerted by the cell to deform the substrate is then calculated as the time rate of change of U_s.

Measurement of the Young's Modulus of the Gel. The Young modulus is determined by measuring the static indentation depth Δz of a tungsten carbide sphere (R = 150 μm, W = 1.898 μN, Hoover Precision, East Gramby, CT, USA) slowly deposited on the substrate. Keer (4) found the following equation relating the Young modulus, E, of a slab of gel of thickness h, the indentation depth ζ and the radius R and apparent weight W of the sphere,

$$E = \frac{3(1-\sigma^2)WR}{4a_0^3}, \qquad \text{[SI7]}$$

where the Poisson ratio is assumed σ = 0.3 (5) and a_0 is solved from

$$\zeta = \frac{a_0^{\,2}}{R}\left[1 - 0.504(a_0/h) - 0.225(a_0/h)^3 - 0.098(a_0/h)^5\right]. \qquad \text{[SI8]}$$

We determine ζ as the depth where the beads displaced by the carbide sphere come into focus in a z-stack of images with a distance between focal planes of $\Delta z = 0.4\ \mu m$. The in-focus beads are detected using the SOBEL function in MATLAB. The Young moduli recorded in our experiments range between 540 and 1400 Pa, with an average of 910 Pa and a standard deviation of 360 Pa.

Determination of the Average Distance, h-h_0, Between the Displacement Marker Particles and the Free Surface of the Substrate. We use z-stacks with $\Delta z = 0.4\ \mu m$ recording the cells in the DIC channel and the marker-particles in the fluorescent channel. The free surface of the gel is defined as the plane where the cell outlines have a maximum number of in-focus pixels. The average depth of the markers is determined to maximize the number of in-focus beads using the SOBEL function in MATLAB (Mathworks Inc, Natick, MA) and an interpolation procedure that yields resolutions finer than Δz. The gaps recorded in our experiments range from 0 to $0.4\ \mu m$. We have used the conservative value h-$h_0 = 0.4\ \mu m$ in the calculation of the forces.

Distortion of the vertical position of the marker particles due to image blurring. As we have shown in Figs. 1-2, the distance between the displacement marker particles

and the free surface of the substrate has an important effect on the fine-scale features of the measured traction forces. In our experiments, this distance can be easily defined by selecting the focal plane where the marker particles are imaged. However, the light generated by out-of-focus particles "leaks" into the selected focal plane and introduces uncertainties in the vertical position of the displacement markers. Hence, the focal plane has to be selected carefully to avoid systematic errors in the vertical position of the marker particles.

Figure SI5A sketches this phenomenon. The intensity of a spherical marker in an *xz* image obtained with a Z-stack is more similar to a "blurred hourglass" than to an ideal circle. The blurring of the imaged marker particles leads to an apparent profile of particles (red line in Fig. SI5A) much more spread than their actual distribution (blue line in Fig. SI5A). This effect can be represented mathematically as the convolution of the ideal image with the point-spread function (PSF) of the marker particles (6). Here, we are only concerned with distortions of the brightness field, *b(z)*, in the vertical direction,

$$b(z) = \int_0^h N(\zeta) PSF(z-\zeta)\, d\zeta, \qquad \text{[SI9]}$$

where $N(\zeta)$ is the distribution of beads along z. The shape of the PSF along the vertical axis is rather complex (7, 8) but for our purposes it can be roughly modeled as a Gaussian as we will show below. To first approximation, the shape of $N(\zeta)$ is irrelevant for our estimations provided that $N(\zeta)$ is much narrower than the PSF. Figure SI5B shows that this condition is fulfilled in our experiments. The black circles in that figure represent profiles of the fluorescence intensity coming from the marker particles as a function of *z-h*. The intensity profile penetrates around 2 microns into the subspace z>0, where there are no beads, indicating that the PSF is indeed much wider than the distribution of beads. We have chosen $N(\zeta)$ to be a Normal distribution centered at $z=h_0$ to provide simple analytical estimations but similar results have been obtained numerically for other distributions, including more realistic cases where $N(\zeta>0) = 0$. Using the functions proposed above we have that

$$b(z) \approx \frac{e^{-\frac{h_0^2}{\delta^2}}}{\pi\delta d} \int_{-\infty}^{\infty} \exp\left[-\frac{(\zeta-h_0)^2}{\delta^2}\right] \exp\left[-\frac{(\zeta-z)^2}{d^2}\right] d\zeta = \frac{e^{-\frac{h_0^2}{\delta^2}} e^{-\frac{(z-h_0)^2}{\delta^2+d^2}}}{\sqrt{\pi}\sqrt{\delta^2+d^2}}, \qquad \text{[SI10]}$$

which becomes

$$b(z) \propto e^{-\frac{(z-h_0)^2}{d^2}} \qquad \text{[SI11]}$$

in the limit $d>>\delta$, when $N(\zeta)$ tends to a Dirac's delta. This result indicates that the brightness distribution is approximately equal to the PSF with its origin at the average position of the marker particles. The brightness distribution shown in Fig. SI5B supports this idea. Equation SI11 implies that the marker particles have to be imaged at the plane where their fluorescence brightness is maximum in order to cancel systematic errors in their vertical location. This can be understood simply by observing the diagram in Fig. SI5A. If a focal plane $z=z_1 \neq h_0$ was selected, most of the information of particle displacements would be coming from particles at a different vertical position. In our experiments, we have always imaged the marker particles at the plane where their brightness is maximum to minimize the systematic errors in their vertical position.

Appendix B
Solution of the elastostatic equation in a substrate of finite thickness

We consider a cell moving on the free surface of a linearly elastic substrate of finite thickness h. We adopt a Cartesian coordinate system with the x and y axes parallel to the base of the substrate, which is located at $z = 0$. When the cell adheres to the elastic substrate and migrates, it induces a displacement field $\mathbf{u} = (u, v, w)$ whose lateral components are measured on a given horizontal plane by seeding the substrate with particle-markers and tracking their displacements. The measurement plane is located some finite distance from the surface, $z = h_0$. Figure SI3 sketches this configuration.

The equations governing the displacement field are

$$\frac{\nabla(\nabla \cdot \mathbf{u})}{(1-2\sigma)} + \Delta\mathbf{u} = 0. \tag{1}$$

The boundary conditions can be partially set by imposing zero displacements at the base of the substrate,

$$\mathbf{u}(x, y, 0) = 0, \tag{2}$$

since the solid glass beneath the substrate is infinitely rigid. A second set of conditions are imposed from the displacements measured at $z = h_0$,

$$u(x, y, h_0) = u^{h0}(x, y),\ v(x, y, h_0) = v^{h0}(x, y). \tag{3}$$

The remaining boundary condition is that the vertical tensile stresses on the surface of the substrate are zero,

$$\tau_{zz}(x, y, h) = 0. \tag{4}$$

This is a reasonable assumption since the weight of the cell is negligibly small due to the similar densities of the cells and their surrounding buffer fluid, and because the force-generating elements of the cytoskeleton have a predominant horizontal orientation.

The solution of the problem (1-4) is sought by expressing the displacements in Fourier series,

$$(u, v, w) = \sum_{\alpha=-\infty}^{\infty} \sum_{\beta=-\infty}^{\infty} [\widehat{u}_{\alpha,\beta}(z), \widehat{v}_{\alpha,\beta}(z), \widehat{w}_{\alpha,\beta}(z)] \exp(\mathrm{i}\alpha x) \exp(\mathrm{i}\beta y), \tag{5}$$

where α and β are the wavenumbers in the x and y directions, and $\widehat{u}_{\alpha,\beta}$, $\widehat{v}_{\alpha,\beta}$ and $\widehat{w}_{\alpha,\beta}$ are the complex Fourier coefficients of u, v and w. Introducing (5) into (1), we obtain the following first-order ordinary differential equation for the z functional form of these Fourier coefficients,

$$\frac{d}{dz}\begin{bmatrix} \widehat{u}_{\alpha,\beta} \\ \widehat{v}_{\alpha,\beta} \\ \widehat{w}_{\alpha,\beta} \\ \widehat{du}_{\alpha,\beta}/dz \\ \widehat{dv}_{\alpha,\beta}/dz \\ \widehat{dw}_{\alpha,\beta}/dz \end{bmatrix} = \frac{d\widehat{\mathbf{u}}_{\alpha,\beta}}{dz} = A_{\alpha,\beta}\widehat{\mathbf{u}}_{\alpha,\beta}, \tag{6}$$

whose matrix is given by

$$A_{\alpha,\beta} = \begin{bmatrix} 0 & 0 & 0 & 1 & 0 & 0 \\ 0 & 0 & 0 & 0 & 1 & 0 \\ 0 & 0 & 0 & 0 & 0 & 1 \\ \frac{2\alpha^2(1-\sigma)+\beta^2(1-2\sigma)}{1-2\sigma} & \frac{\alpha\beta}{1-2\sigma} & 0 & 0 & 0 & \frac{-\mathrm{i}\alpha}{1-2\sigma} \\ \frac{\alpha\beta}{1-2\sigma} & \frac{2\beta^2(1-\sigma)+\alpha^2(1-2\sigma)}{1-2\sigma} & 0 & 0 & 0 & \frac{-\mathrm{i}\beta}{1-2\sigma} \\ 0 & 0 & \frac{(\alpha^2+\beta^2)(1-2\sigma)}{2(1-\sigma)} & \frac{-\mathrm{i}\alpha}{2(1-\sigma)} & \frac{-\mathrm{i}\beta}{2(1-\sigma)} & 0 \end{bmatrix}.$$

This matrix has two eigenvalues, $\lambda = \pm k^2 = \pm(\alpha^2+\beta^2)$, with algebraic multiplicity equal to 3 and geometric multiplicity equal to 2. The matrix of eigenvectors is

$$M_{\alpha,\beta} = \begin{bmatrix} \alpha^2 & \mathrm{i}\alpha & -\beta/k & \mathrm{i} & \mathrm{i}\alpha & \alpha\beta \\ \alpha\beta & \mathrm{i}\beta & \alpha/k & 0 & \mathrm{i}\beta & \beta^2 \\ -\mathrm{i}\alpha k & 4k\,(1-\sigma) & 0 & -\alpha/k & -4k\,(1-\sigma) & \mathrm{i}\beta k \\ \alpha^2 k & 0 & -\beta & -\mathrm{i}k & 0 & -\alpha\beta k \\ \alpha\beta k & 0 & \alpha & 0 & 0 & -k\beta^2 \\ -\mathrm{i}\alpha k^2 & k^2\,(3-4\sigma) & 0 & \alpha & k^2\,(3-4\sigma) & -\mathrm{i}\beta k^2 \end{bmatrix}$$

and its associated Jordan form is

$$J_{\alpha,\beta} = M_{\alpha,\beta}^{-1} A_{\alpha,\beta} M_{\alpha,\beta} = \begin{bmatrix} k & -\mathrm{i}k/\alpha & 0 & 0 & 0 & 0 \\ 0 & k & 0 & 0 & 0 & 0 \\ 0 & 0 & k & 0 & 0 & 0 \\ 0 & 0 & 0 & -k & 0 & 0 \\ 0 & 0 & 0 & 0 & -k & 0 \\ 0 & 0 & 0 & 0 & -\mathrm{i}k/\beta & k \end{bmatrix}.$$

The solution of the differential equation (6) is

$$\widehat{\mathbf{u}}_{\alpha,\beta}(z) = M_{\alpha,\beta} \exp(J_{\alpha,\beta} z) M_{\alpha,\beta}^{-1} \widehat{\mathbf{u}}^0_{\alpha,\beta}, \tag{7}$$

where $\widehat{\mathbf{u}}^0_{\alpha,\beta}$ is the boundary value of $\widehat{\mathbf{u}}_{\alpha,\beta}$ at $z=0$, which can be written as

$$\widehat{\mathbf{u}}^0_{\alpha,\beta} = \begin{bmatrix} 0 \\ 0 \\ 0 \\ du^0_{\alpha,\beta} \\ dv^0_{\alpha,\beta} \\ dw^0_{\alpha,\beta} \end{bmatrix}.$$

Notice that this expression already includes the boundary condition (2). The constants $du^0_{\alpha,\beta}$, $dv^0_{\alpha,\beta}$ and $dw^0_{\alpha,\beta}$ represent the z-derivatives of the Fourier coefficients of the displacements at $z=0$. After some algebra manipulation one obtains

$$\widehat{\mathbf{u}}_{\alpha,\beta}(z) = \begin{bmatrix} \frac{\left[(3-4\sigma)\alpha^2-4(1-\sigma)\beta^2\right]\sinh(kz)}{4k^3(1-\sigma)} - \frac{\alpha^2 z\cosh(kz)}{4k^2(1-\sigma)} \\ -\frac{\beta\alpha\sinh(kz)}{4k^3(1-\sigma)} + \frac{\beta\alpha z\cosh(kz)}{4k^2(1-\sigma)} \\ \frac{-\mathrm{i}\sinh(kz) z\alpha}{(1-\sigma)k} \\ \frac{\alpha^2 z\sinh(kz)}{4(1-\sigma)k} + \cosh(kz) \\ \frac{\beta\alpha z\sinh(kz)}{4(1-\sigma)k} \\ -\frac{\mathrm{i}\alpha\sinh(kz)}{4(1-\sigma)k} - \frac{\mathrm{i}\alpha z\cosh(kz)}{4(1-\sigma)} \end{bmatrix} du^0_{\alpha,\beta} + \\ + \begin{bmatrix} -\frac{\beta\alpha\sinh(kz)}{4k^3(1-\sigma)} + \frac{\beta\alpha z\cosh(kz)}{4k^2(1-\sigma)} \\ \frac{\left[(3-4\sigma)\beta^2-4(1-\sigma)\alpha^2\right]\sinh(kz)}{4k^3(1-\sigma)} - \frac{\beta^2 z\cosh(kz)}{4k^2(1-\sigma)} \\ \frac{-\mathrm{i}\sinh(kz) z\alpha}{(1-\sigma)k} \\ \frac{\beta\alpha z\sinh(kz)}{4(1-\sigma)k} \\ \frac{\beta^2 z\sinh(kz)}{4(1-\sigma)k} + \cosh(kz) \\ -\frac{\mathrm{i}\beta\sinh(kz)}{4(1-\sigma)k} - \frac{\mathrm{i}\beta z\cosh(kz)}{4(1-\sigma)} \end{bmatrix} dv^0_{\alpha,\beta} +$$

$$+\begin{bmatrix} \frac{-\mathrm{i}\alpha z\sinh(kz)}{2k(1-2\sigma)} \\ -\frac{\mathrm{i}\beta z\sinh(kz)}{2k(1-2\sigma)} \\ \frac{(3-4\sigma)\sinh(kz)}{2k(1-2\sigma)} - \frac{z\cosh(kz)}{2(1-2\sigma)} \\ -\frac{\mathrm{i}\alpha\sinh(kz)}{2k(1-2\sigma)} - \frac{\mathrm{i}\alpha z\cosh(kz)}{2(1-2\sigma)} \\ -\frac{\mathrm{i}\beta\sinh(kz)}{2k(1-2\sigma)} - \frac{\mathrm{i}\beta z\cosh(kz)}{2(1-2\sigma)} \\ -\frac{kz\sinh(kz)}{2(1-2\sigma)} + \cosh(kz) \end{bmatrix} dw^0_{\alpha,\beta}. \tag{8}$$

The constants $du^0_{\alpha,\beta}$, $dv^0_{\alpha,\beta}$ and $dw^0_{\alpha,\beta}$ have to be determined using the boundary conditions (3) and (4). To impose (4), we use the constitutive law that relates the Fourier coefficients of the vertical tensile stresses to those of the displacements,

$$\widehat{\tau_{zz}}_{\alpha,\beta}(h) = \frac{E}{(1+\sigma)(1-2\sigma)}\left[\frac{d\widehat{w}_{\alpha,\beta}}{dz}(h) + \mathrm{i}\sigma\left(\alpha\widehat{u}_{\alpha,\beta}(h) + \beta\widehat{v}_{\alpha,\beta}(h)\right)\right]. \tag{9}$$

Evaluating equation (8) at h_0 and h, and using the above expression to impose the boundary condition (4), we obtain the following 3×3 linear system of equations,

$$B_{\alpha,\beta}\begin{bmatrix} du^0_{\alpha,\beta} \\ dv^0_{\alpha,\beta} \\ dw^0_{\alpha,\beta} \end{bmatrix} = \begin{bmatrix} \widehat{u}^{h0}_{\alpha,\beta} \\ \widehat{v}^{h0}_{\alpha,\beta} \\ 0, \end{bmatrix}, \tag{10}$$

where $(\widehat{u}^{h0}_{\alpha,\beta}, \widehat{v}^{h0}_{\alpha,\beta})$ are the Fourier coefficients of the measured displacements at $z=h_0$ he solution of this system yields the three unknown coefficients needed to obtain the displacements, effectively closing the problem. The matrix $B_{\alpha,\beta}$ is

$$B_{\alpha,\beta} = \begin{bmatrix} \frac{\alpha^2 kh_0\,\mathrm{C}(kh_0) - \left[(3-4\sigma)\alpha^2 - 4(1-\sigma)\beta^2\right]\mathrm{S}(kh_0)}{4k^3(1-\sigma)} & \frac{\alpha\beta[kh_0\,\mathrm{C}(kh_0) - \mathrm{S}(kh_0)]}{4k^3(1-\sigma)} & -\frac{\mathrm{i}\alpha h_0\,\mathrm{S}(kh_0)}{2k(1-2\sigma)} \\ \frac{\alpha\beta[kh_0\,\mathrm{C}(kh_0) - \mathrm{S}(kh_0)]}{4k^3(1-\sigma)} & \frac{\beta^2 kh_0\,\mathrm{C}(kh_0) - \left[(3-4\sigma)\beta^2 - 4(1-\sigma)\alpha^2\right]\mathrm{S}(kh_0)}{4k^3(1-\sigma)} & -\frac{\mathrm{i}\beta h_0\,\mathrm{S}(kh_0)}{2k(1-2\sigma)} \\ -\frac{\mathrm{i}\alpha(1-2\sigma)[(1-2\sigma)\,\mathrm{S}(kh) + kh\,\mathrm{C}(kh)]}{k(1-\sigma)} & -\frac{\mathrm{i}\alpha(1-2\sigma)[(1-2\sigma)\,\mathrm{S}(kh) + kh\,\mathrm{C}(kh)]}{k(1-\sigma)} & \frac{2(1-\sigma)\,\mathrm{C}(kh) - kh\,\mathrm{S}(kh)}{2} \end{bmatrix}.$$

In the above expression, the symbols C and S stand for cosh and sinh respectively. The solution of the linear system (10) closes the problem by providing the unknowns that are required to determine $\widehat{\mathbf{u}}_{\alpha,\beta}(z)$ in (7).

The Fourier coefficients of the tangential stress field on the surface of the substrate are related to $\widehat{\mathbf{u}}_{\alpha,\beta}(z)$ through the constitutive equations

$$\widehat{\tau_{xz}}_{\alpha,\beta}(h) = \frac{E}{2(1+\sigma)}\left[\frac{d\widehat{u}_{\alpha,\beta}}{dz}(h) + \mathrm{i}\alpha\widehat{w}_{\alpha,\beta}(h)\right], \tag{11}$$

$$\widehat{\tau_{yz}}_{\alpha,\beta}(z) = \frac{E}{2(1+\sigma)}\left[\frac{d\widehat{v}_{\alpha,\beta}}{dz}(h) + \mathrm{i}\beta\widehat{w}_{\alpha,\beta}(h)\right]. \tag{12}$$

The inverse Fourier transform of these coefficients yields the traction field on the surface of the substrate,

$$(\tau_{xz},\tau_{yz})(h) = \frac{1}{(2\pi)^2}\sum_{\alpha=-\infty}^{\infty}\sum_{\beta=-\infty}^{\infty}\left[\widehat{\tau_{xz}}_{\alpha,\beta}(h), \widehat{\tau_{yx}}_{\alpha,\beta}(h)\right]\exp(-\mathrm{i}\alpha x)\exp(-\mathrm{i}\beta y).$$

We now present the asymptotic behavior of the solution for very high wavenumbers, $kh_0 \gg 1$. In this limit, the solution in (8) becomes

$$\widehat{\mathbf{u}}_{\alpha,\beta}(z) \sim h\exp(kh)\begin{bmatrix} 0 \\ 0 \\ 0 \\ du^0_{\alpha,\beta} \\ dv^0_{\alpha,\beta} \\ dw^0_{\alpha,\beta} \end{bmatrix}. \tag{13}$$

A more detailed analysis is required for $B_{\alpha,\beta}$, which becomes

$$B_{\alpha,\beta} \sim h_0 e^{kh_0} \begin{bmatrix} \frac{\alpha^2 - \left[(3-4\sigma)\alpha^2 - 4\beta^2(1-\sigma)\right]\epsilon}{4k^2(1-\sigma)} & \frac{\beta\alpha(1-\epsilon)}{4k^2(1-\sigma)} & \frac{-\mathrm{i}\alpha}{2k(1-\sigma)} \\ \frac{\beta\alpha(1-\epsilon)}{4k^2(1-\sigma)} & \frac{\beta^2 - \left[(3-4\sigma)\beta^2 - 4\alpha^2(1-\sigma)\right]\epsilon}{4k^2(1-\sigma)} & \frac{-\mathrm{i}\beta}{2k(1-\sigma)} \\ \frac{-\mathrm{i}\alpha h(1-2\sigma)\exp[k(h-h_0)][1+(1-2\sigma)\epsilon]}{kh_0(1-\sigma)} & \frac{-\mathrm{i}\alpha h(1-2\sigma)\exp[k(h-h_0)][1+(1-2\sigma)\epsilon]}{kh_0(1-\sigma)} & \frac{h\exp[k(h-h_0)][2(1-\sigma)\epsilon-1]}{2h_0} \end{bmatrix}.$$

The small parameter $\epsilon = (kh_0)^{-1}$ has been kept in the above expression because $B_{\alpha,\beta}$ is singular at leading order. For $\epsilon \ll 1$, the solution of (10) is written as

$$\begin{bmatrix} du^0_{\alpha,\beta} \\ dv^0_{\alpha,\beta} \\ dw^0_{\alpha,\beta} \end{bmatrix} \sim [h_0 \exp(kh_0)]^{-1} \left(\frac{1}{\epsilon}\right) \sim \frac{\exp(-kh_0)}{k}.$$

Combining this expression with (13), we finally get a simple formula that relates the displacements at $z = h$ with those measured at $z = h_0$,

$$\widehat{\mathbf{u}}_{\alpha,\beta}(h) \sim kh \exp\left[k(h-h_0)\right] \widehat{\mathbf{u}}_{\alpha,\beta}(h_0),$$

in the limit $kh_0 \gg 1$. This result shows that the amplitude of the small-scale features of the displacements measured at $z = h_0$ are smaller than those at $z = h$, and that the ratio between these two increases exponentially with the wave number. Using (11), it follows that the traction forces exhibit the same exponential dependence on the distance from the substrate of the gel to the measurement plane $(h - h_0)$.

Supplementary Figures

Fig. SI1

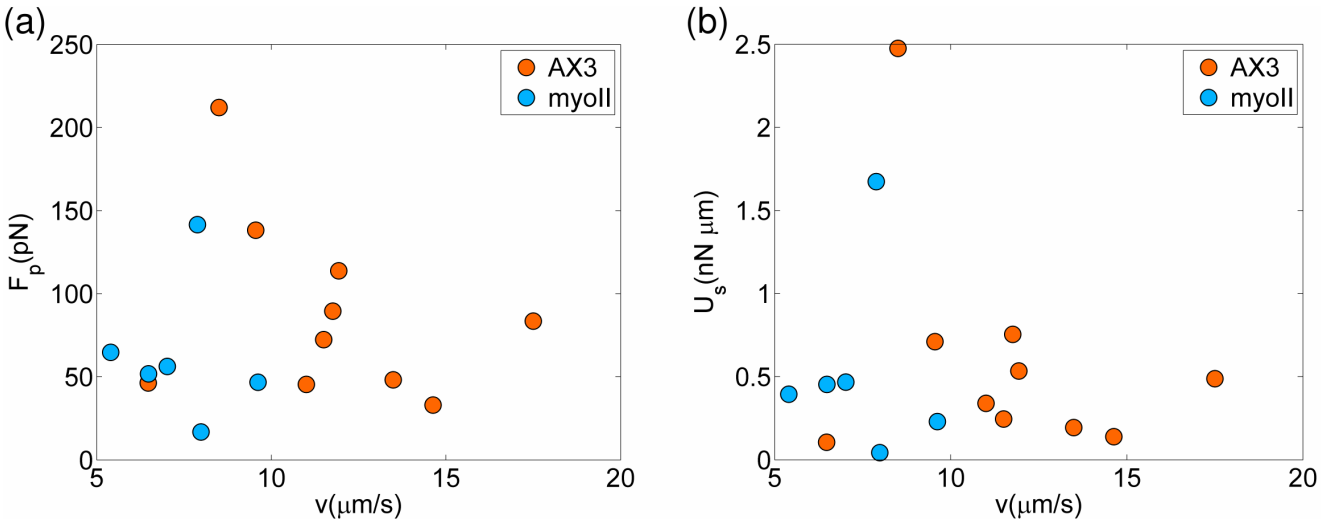

Caption for Figure SI1

Scatter plots of the average translation velocity of each cell (v) versus the average magnitude of the pole forces (F_p, panel a) or the average value of the strain energy (U_s, panel b). Orange symbols represent wild-type cells (N=10) and blue symbols represent *myoII*$^-$ cells (N=6). The data show little correlation between v and F_p or U_s.

Fig. SI2

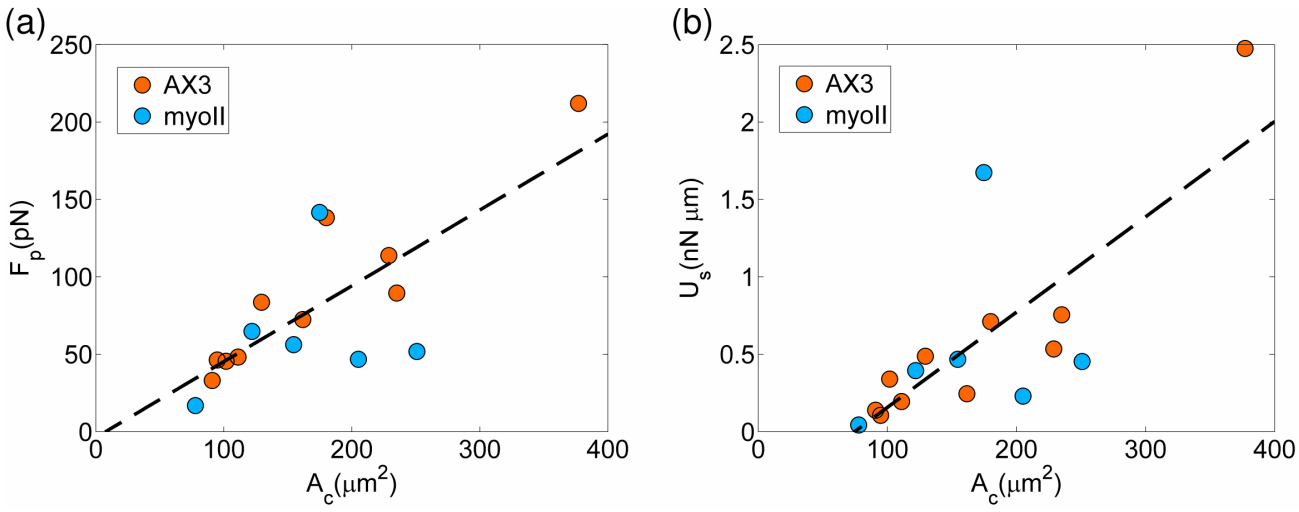

Caption for Figure SI2

Scatter plots of the average translation horizontal projected area of each cell (A_c) versus the average magnitude of the pole forces (F_p, panel a) or the average value of the strain energy (U_s, panel b). Orange symbols represent wild-type cells (N=10) and blue symbols represent *myoII*- cells (N=6). The data show strong correlation between A_c and F_p or U_s. The dashed lines are least square fits to the data: $F_p = 0.49\ pN/\mu m^2 \times (Ac - 7.5\ \mu m^2)$ and $U_s = 0.0062\ nN/\mu m \times (Ac - 75\ \mu m^2)$.

Fig.SI3

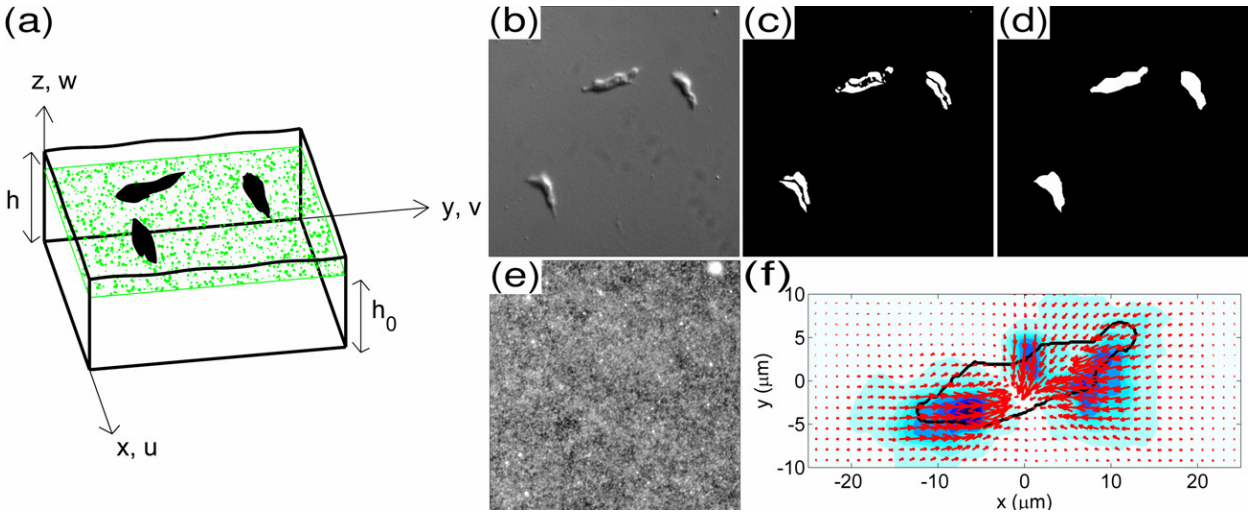

Caption for Figure SI3

Illustration of the traction cytometry method. (A) Sketch of the experimental configuration. (B) Example of a raw DIC image used for cell contour identification. (C) The same DIC image corrected with the session average and a threshold applied to select the most intense regions. (D) Final cell contours obtained. (E) Example of a GFP image used to determine the deformation of the substrate. (F) Displacement field obtained for a crawling Dictyostelium cell. The arrows indicate the intensity and direction of the vector data. The color contours indicate their intensity.

Figure SI4

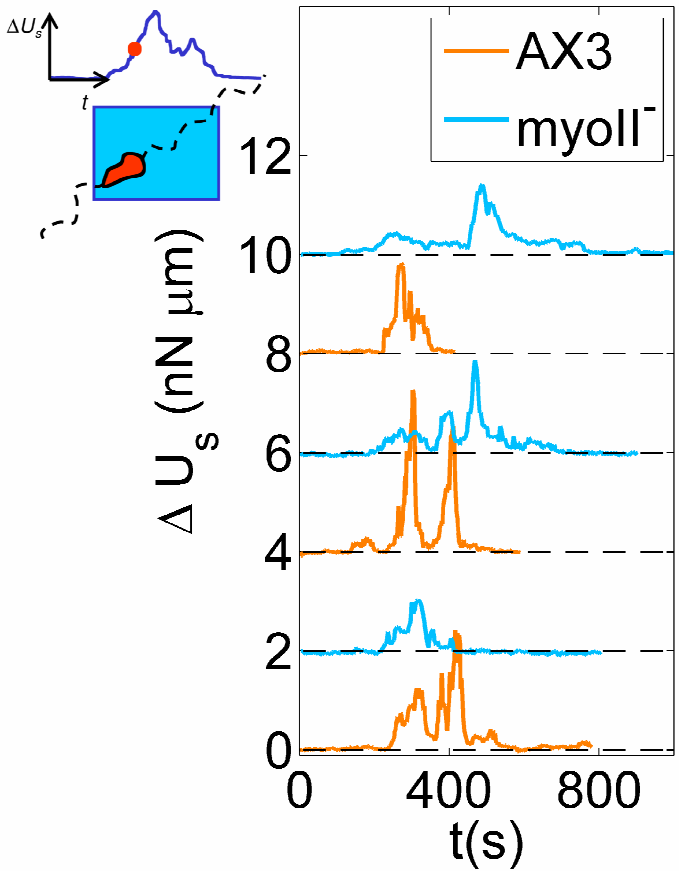

Caption for Figure SI4

Elastic recovery of the gelatin gels used in our experiments. Each curve shows a time history of the deformation energy of in square domain of the substrate that is crossed by a cell. The initial value of the energy has been subtracted so that $\Delta U_s(t) = U_s(t) - U_s(0)$ and the baseline level is $\Delta U_s = 0$. The curves have been stacked in the Y axis with a separation of 2 nN μm between each two of them. The data come from different cells and different gel preparations. Initially, the domain is empty and the deformation energy is at its baseline. When the cell enters the domain, the deformation energy rises and it finally returns to its baseline after the cell leaves the domain.

Figure SI5

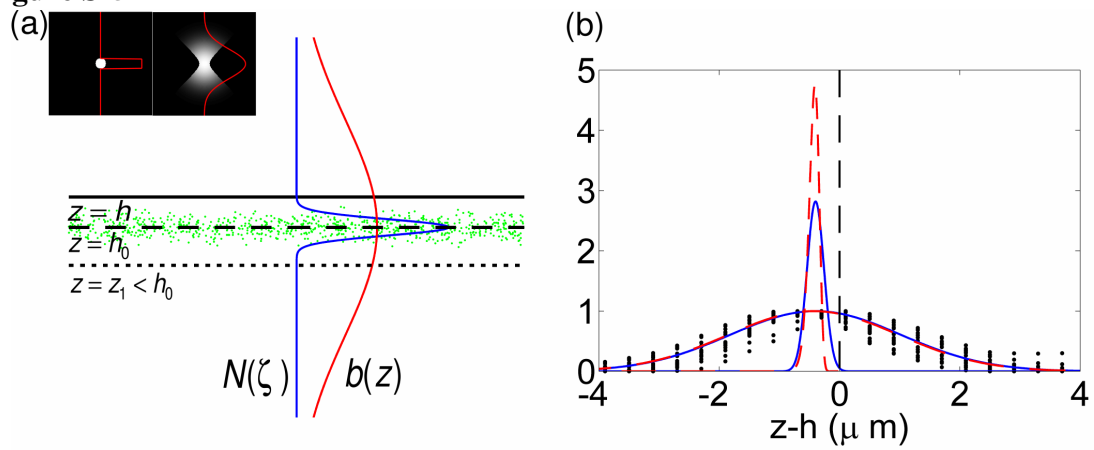

Caption for Figure SI5

Distortion of the vertical position of the marker particles used to measure the traction forces due to image blurring. a) Sketch of this phenomenon. The intensity of a spherical marker in an *xz* image obtained with a Z-stack is more similar to a "blurred hourglass" than to an ideal circle. This leads to an apparent profile of particles (*b(z)*, red line) that is much more spread than their actual distribution (*N(z),* blue line). The peak of the intensity profile coincides with the average of *N(z),* so that the systematic error in the vertical position of the markers is cancelled when the focal plane selected to visualize the marker particles is $z=h_0$. If the focal plane $z=z_1 \neq h_0$ was selected, most of the information of particle displacements would be coming from particles at a different vertical position. b) The black circles are intensity profiles coming from squares of size 40 μm in our gels, represented as a function of *z-h*. The color curves represent our model equations for *N(z)* and *b(z).* The solid, blue curves have been obtained using a Normal distribution with μ=-0.4 and σ=0.2 microns. The dashed, red curves have been obtained using a Log-Normal distribution with μ =-1 and σ=0.2 microns. In both cases, the PSF is a Gaussian with a *1/e* radius of 2 microns.

Movies

These movies show moving *Dictyostelium* cells. They have been produced by overlaying the results from our force calculations at each instant of time on the DIC image recorded at that same instant of time. The black contour is the outline of the cell. The color contours map the magnitude of the stresses that the cell exerts on the substrate. The red and orange arrows indicate the magnitude and direction of the front and back pole forces. The reference arrow at the lower left corner represents a force of 100 pN. The reference bar at the same location is 10 μm long. The plot at the upper right corner of each panel shows the time evolution of the strain energy of the substrate for the selected images. The red circle in that plot indicates the instant of time that corresponds to each frame. The duration of each movie depends on the period of time that each cell remains on the field of view of the microscope. Movies 1-2 show wild-type cells and their time resolution of 2 seconds. Movies 3-4 show *myoII*$^{-}$ cells with a time resolution of 2 seconds.

1. Robinson, D. N. & Spudich, J. A. (2000) *J Cell Biol* **150,** 823-38.
2. Willert, C. E. & Gharib, M. (1991) *Exp Fluids* **10,** 181-193.
3. William H. Press, S. A. T., William T. Vetterling and Brian P. Flannery (1992) *Numerical recipes in FORTRAN: the art of scientific computing* (Cambridge University Press, New York, NY, USA.).
4. Keer, L. M. (1964) *J. Mech. Physics Solids* **12,** 149-163.
5. Li, Y., Hu, Z. & Li, C. (1993) *J. Appl. Polymer Sci.***,** 1107-1111.
6. Greenfield Sluder & Wolf, D. E. (2003) in *Methods in Cell Biology*, ed. Matsudaira, L. W. a. P. (Elsevier, San Diego), Vol. 72.
7. Gibson, S. F. & Lanni, F. (1991) *Journal of the Optical Society of America a-Optics Image Science and Vision* **8,** 1601-1613.
8. McNally, J. G., Preza, C., Conchello, J. A. & Thomas, L. J. (1994) *Journal of the Optical Society of America a-Optics Image Science and Vision* **11,** 1056-1067.